Renewable resources derived hyperbranched polyurethane/aluminium hydroxide decorated reduced graphene oxide nanocomposite

Highlight

The current chapter describes the formation of nanocomposite of renewable resource derived hyperbranched polyurethane (HPU) with aluminium hydroxide-decorated reduced graphene oxide nanohybrid (AH@rGO). Fabrication of the nanocomposite was performed by *in situ* polymerization using four different loadings (0.3, 0.5, 1.0 and 2.0 wt%) of the AH@rGO nanohybrid. The nanohybrid and fabricated nanocomposites were characterized by various spectroscopic, microscopic and analytical techniques. The nanocomposites exhibited remarkable enhancement in mechanical properties *viz.* tensile strength (~350%), elongation at break (~292%) and toughness (~441%), in comparison to the pristine polymer. The nanocomposite system showed high thermal stability (initial degradation temperatures upto 315 °C). The nanocomposites also demonstrated excellent multi-stimuli triggered shape memory attributes under thermal energy (60 °C), microwave (300 W) and direct sunlight. Both the polymer matrix and the nanohybrid contributed to the overall performance of the nanocomposite. The performance of the nanocomposite was found to be dose-dependent on the nanomaterial loading. The development of such high performance nanocomposite holds good potential for shape memory applications.

Portions of this chapter are published in:

Bayan, R. and Karak, N. Renewable resource derived aliphatic hyperbranched polyurethane/aluminium hydroxide–reduced graphene oxide nanocomposites as robust, thermostable material with multi-stimuli responsive shape memory features. *New Journal of Chemistry*, 41(17):8781-8790, 2017.

3.1. Introduction

As discussed in **Chapter 1**, renewable resource based PUs are successful in imparting desirable attributes like biodegradability and biocompatibility, which can help combat the global polymer crisis. However, such PUs require occasional modifications in a bid to cater to the modern-day demands, in terms of properties and applications. In this context, nanotechnology based approach is found to be convenient for addressing the inadequacies of renewable resource based PUs. Nanocomposite formation provides a simple and effective route to overcome the shortcomings of pristine polymers. In recent time, much attention has been drawn by polymer nanocomposites with carbon based nanomaterials. Assimilation of such strong, highly potent nanoparticles, sheets or tubes in the polymer matrix can generate high performance nanocomposites which can be customized for in-demand applications [1]. In this milieu, graphene, a two dimensional planar system of hexagonally connected sp^2 hybrid carbon atoms is an excellent material for building such high performance polymeric materials [2]. Incorporation of graphene in the polymer matrix can efficiently augment mechanical, thermal, and electrical properties for such nanocomposites [3, 4]. Thus, such graphene based polymer nanocomposites have promising prospect for the development of robust, durable and multi-functional materials with minimum nanomaterial quantity. Literature cites numerous examples of graphene based PUNCs. Kim et al. reported improvement in electrical conductivity and gas barrier properties of exfoliated graphene/PUNCs [5]. Strankowski et al. reported enhancement of mechanical and thermal properties of PU/graphene nanocomposite [6]. Over the years, graphene-hybrid composites are also evolving towards the formation of high performance PUNC. Ceramic–graphene composites have been reported as highly efficient chemical sensors [7]. Silicon-graphene composites have found use as reversible lithium storage [8]. Recently, alumina based graphene composites have been used as electrically conductive materials for high temperature application [9].

Among its myriad qualities, PU is well known as a shape memory polymer (SMP), as discussed in the previous chapters. They show the ability of altering a predetermined shape to its original shape in response to an appropriate stimulus [10]. Owing to its high recoverable strain (up to 400%), wide transition temperature range of shape recovery, high control of retraction and softening temperatures, tunable soft–hard segments, etc. PU has been widely used in the development of SMPs [11, 12]. Although shape memory activity by direct heating is the most common, other stimuli like magnetic field, light, microwave, etc. have also been successfully applied [13]. However, one of the major impediments of SMPs is their small recovery force (due to low stiffness of SMPs). Moreover, most SMPs poorly

responded under such stimuli due to the poor thermal conductivity of these materials. Thus, robust and good thermal conductive nanomaterials are required to improve uniform heat transfer ability to the SMP matrix, thereby facilitating efficient remote heating and also competently reinforcing the matrix in the process. In this juncture, PUNC with carbon based nanomaterials like graphene is an ideal approach. This is due to excellent thermal conductivity, electrical conductivity, light absorbing capacity, etc. of graphene, apart from imparting strength to the polymer matrix [14]. Literature reports have abundantly featured such PU/graphene nanocomposites as efficient shape memory materials [14-17].

In this endeavour, the fabrication of renewable resource based HPU nanocomposite (HPUNC) with aluminium hydroxide-reduced graphene oxide (AH@rGO) nanohybrid was reported. Different weight percentages of the nanohybrid were used to prepare HPUNCs by *in situ* polymerization technique. Both the nanohybrid and nanocomposites were characterized by using various spectroscopic and microscopic tools. Mechanical and thermal properties of the nanocomposites were evaluated. The fabricated nanocomposites were tested for shape memory attribute under exposure of different external stimuli like thermal energy, microwave and sunlight.

3.2. Experimental

3.2.1. Materials

PCL, IPDI, MGE, COMP and xylene were used for the preparation of HPUNC. Molecular sieves were used to store the solvents. All these chemicals possess the same grade and specifications as described in Chapter 2 (Section 2.2.1).

Graphite was used as the precursor for preparation of GO. It is the most stable carbon allotrope under ambient conditions, possessing a layered honeycomb structure of planar hexagonally arranged carbon atoms. Graphite flakes (60 mesh, 99% purity) were procured from Loba Chemie, India and used as received.

Concentrated sulphuric acid (conc. H_2SO_4) was used as an oxidant for the preparation of GO. It is a strong acid with molar mass of 98.07 g mol^{-1} and density of 1.84 g cm^{-3}. H_2SO_4 (98% v/v) was obtained from Merck, India and used as received.

Potassium permanganate ($KMnO_4$) was used as an oxidant for the preparation of GO. It is a strong oxidizing agent having molar mass of 158.034 g mol^{-1} and density of 2.703 g cm^{-3}. $KMnO_4$ was obtained from Merck, India and used as received.

Hydrogen peroxide (H_2O_2) was used as a precursor in preparation of GO. H_2O_2 was used to reduce the excess permanganate and manganese dioxide to water soluble manganese salt. It is the simplest peroxide with colorless appearance in its neat form. It is a

strong oxidizing agent and possesses bleaching properties. It has a molecular weight of 34.0147 g mol^{-1} and boiling point of 150.2 °C. H_2O_2 (30% v/v) was procured from Merck, India and used as received.

Aluminium sulfate 16-hydrate ($Al_2(SO_4)_3.16H_2O$) was used as a precursor for preparation of aluminium hydroxide-reduced graphene oxide nanohybrid. It is a colorless salt, possessing molar mass of 630.4 g mol^{-1} and density of 2.71 g cm^{-3}. $Al_2(SO_4)_3.16H_2O$ was obtained from Merck, India and used as received.

Dextrose ($C_6H_{12}O_6$) was used as a reducing agent for reduction of GO or rGO. It is a monosaccharide with reducing properties. It has a colorless solid appearance with molar mass of 180.156 g mol^{-1} and density of 1.54 g cm^{-3}. Dextrose (≥99.5%) was acquired from Merck, India and used as received.

N,*N*-dimethylformamide (DMF) was used as a solvent for dispersion of AH@rGO nanohybrid during the preparation of HPUNC. It is a colorless liquid having molar mass of 73.09 g mol^{-1}, boiling point of 153 °C and density of 0.944 g cm^{-3}. DMF was procured from Merck, India and purified by vacuum distillation prior to use.

Dilute hydrochloric acid (dil. HCl) was used for washing and removing of excess manganese salt from GO. It possesses the same grade and specification as described in Chapter 2 (Section 2.2.1).

Ammonia solution (liq. NH_3) was used to maintain a basic pH during the preparation of AH@rGO. It is a weak base, having density of 0.903 g cm^{-3}. Liq. NH_3 (25% w/v) was obtained from Merck, India and used as received.

3.2.2. Methods

3.2.2.1. Preparation of AH@rGO nanohybrid

GO was prepared initially by oxidation of graphite flakes, as per modified Hummers' method [18]. Briefly, 2 g of graphite flakes was subjected to strong acidic treatment with 35 mL of 98% H_2SO_4 under magnetic stirring for 2 h. It was followed by slow and careful addition of 6 g of $KMnO_4$ to the acidified mixture at temperature below 20 °C in an ice-bath. After the addition, the mixture was allowed to attain room temperature and subsequently stirred vigorously at 35 °C for 4 h. Thereafter, the mixture was diluted by stepwise addition of 90 mL of de-ionized water under vigorous stirring for 1 h to give a dark brown suspension. The suspension was further treated with 30% H_2O_2 solution drop wise until the color of the suspension turned bright yellow from dark brown. The bright yellow suspension was separated by centrifugation and purified by repeated washings with 5% aqueous HCl solution to remove excess of manganese salt, followed by de-ionized water until the neutral pH is achieved. After purification, GO was obtained as a brown suspension.

The purified GO was dispersed in de-ionized water by ultrasonication and stored under ambient conditions. For preparation of AH@RGO, GO dispersion in de-ionized water (1 mg mL^{-1}) was mixed with 2.33 g of $Al_2(SO_4)_3.16H_2O$, followed by sonication for 30 minutes. To this salt-aqueous GO dispersion, 25% aqueous NH_3 was added dropwise to adjust the pH to 9, followed by addition of 0.1 g of dextrose. The reactants were subjected to mechanical stirring at 90 °C for 60 min. The resultant dispersion was cooled and the supernatant decanted off to obtain the AH@rGO nanohybrid. The nanohybrid was purified by several washings with water to attain neutral pH and subsequent removal of sulphate ions (tested using $BaCl_2$ solution). The purified AH@rGO nanohybrid was dried in a vacuum oven at 50 °C for 12 h.

3.2.2.2. Fabrication of HPU/AH@rGO nanocomposite

HPU/AH@rGO nanocomposite was fabricated by an *in situ* polymerization technique, using reaction set-up of a three-necked round-bottomed flask, equipped with a mechanical stirrer, a nitrogen gas inlet, a thermometer and a Teflon septum. In brief, PCL and MGE were taken in the reaction flask containing small amount of xylene as a solvent under constant mechanical agitation. After dissolving PCL, IPDI was administered by dropwise addition at room temperature. The reactants were gradually heated to 130±5 °C under constant mechanical agitation and then allowed to react for 3 h, maintaining an NCO/OH ratio of 1.5 in the first step. The highly viscous mass obtained was treated as the pre-polymer. The pre-polymer was cooled to room temperature, followed by sequential addition of the multi-functional moiety COMP, a stable dispersion of AH@rGO (in DMF) and IPDI to the pre-polymer under constant mechanical agitation in the second step. The reactants were gradually re-heated to 130±5 °C and allowed to react for 3 h by maintaining an NCO/OH ratio of 1, till the completion of the reaction as indicated by the formation of a highly viscous mass and confirmed by the absence of free isocyanate (−NCO) band at 2270 cm^{-1} in FT-IR spectrum. HPUNCs with different weight percentages of AH@rGO nanohybrid, *viz.* 0.3 wt%, 0.5 wt%, 1 wt% and 2 wt% were fabricated and encoded as HPU/AH@rGO0.3, HPU/AH@rGO0.5, HPU/AH@rGO1.0 and HPU/AH@rGO2.0 respectively. In the same way, pristine HPU was prepared without using the nanohybrid for comparison purpose. Pristine HPU is HPU3, as described in Chapter 2 and used as the matrix

3.2.2.3. Sample preparation for performance study

HPUNC samples were prepared by the same process as in the case of HPU, as described in Chapter 2 (Section 2.2.2.3). All analyses and testing were performed using bulk HPUNC samples without any further purification.

3.2.2.4. Shape memory study

Shape memory behavior of the HPUNC films was studied by performing spiral bending test. The samples were folded in the form of a spiral shape after heating at 65 °C for 5 min, followed by instant quenching in an ice water-salt bath at 0 °C for 15 min. After attaining the temporary fixed shape, the films were dried under vacuum and then kept at room temperature for 30 min. Thereafter, the shape recovery of the temporary deformed films was achieved under exposure of different stimuli *viz.* thermal energy, microwave and sunlight. The time required for the deformed films to attain original shape was duly noted. The thermal irradiation triggered shape recovery of the films was achieved by directly heating the sample at 60 °C. Similarly, microwave triggered shape recovery was accomplished by placing the sample inside a domestic microwave operating at a power of 300 W. The sunlight induced shape recovery was attained with the samples being exposed directly to sunlight in sunny days of November, 2016, with light intensity of 90000-100000 lux. The shape fixity of the deformed films and their shape recovery were determined by applying Eq. 1.4 and Eq. 1.5, as described earlier in Chapter 1.

3.2.3. Characterization

FT-IR, UV-Vis, XRD, SEM, TGA and DSC analyses of the nanohybrid and HPUNC were performed by the same instruments and under the same conditions as mentioned in Chapter 2 (Section 2.2.3). Raman scattering of the nanohybrid was recorded by a Raman spectrophotometer (Model: Renishaw Basis Series, Renishaw, UK) equipped with 514 nm laser. The size, shape and decoration of the nanohybrid along with its distribution in HPU matrix were visually investigated by using Transmission Electron Microscopy (TEM) instrument (Model: JEM-2100, JEOL, Japan) at an operating voltage of 200 kV using copper grid of Ted Pella Inc., Ultrathin C, Type A, 400 mesh. The TEM images were converted to Fast Fourier Transform (FFT) and Inverse Fast Fourier Transform (IFFT) images by using Gatan Digital Micrograph software. The elemental composition of the nanohybrid was evaluated by Electron Dispersive X-ray (EDX) technique using the same TEM instrument. Various mechanical testing of the HPUNC films *viz.* tensile strength, elongation at break, scratch hardness, impact resistance, etc. were performed by the same instruments and under the same conditions as described in Chapter 2 (Section 2.2.3). The shape memory behavior of HPUNC films was studied by using the same domestic microwave oven, as mentioned in Chapter 2 (Section 2.2.3).

3.3. Results and discussion

3.3.1. Preparation of AH@rGO nanohybrid

AH@rGO nanohybrid was prepared by a one-pot wet chemical reduction technique using dextrose as the bio-based reductant. A probable route is outlined in **Scheme 3.1**.

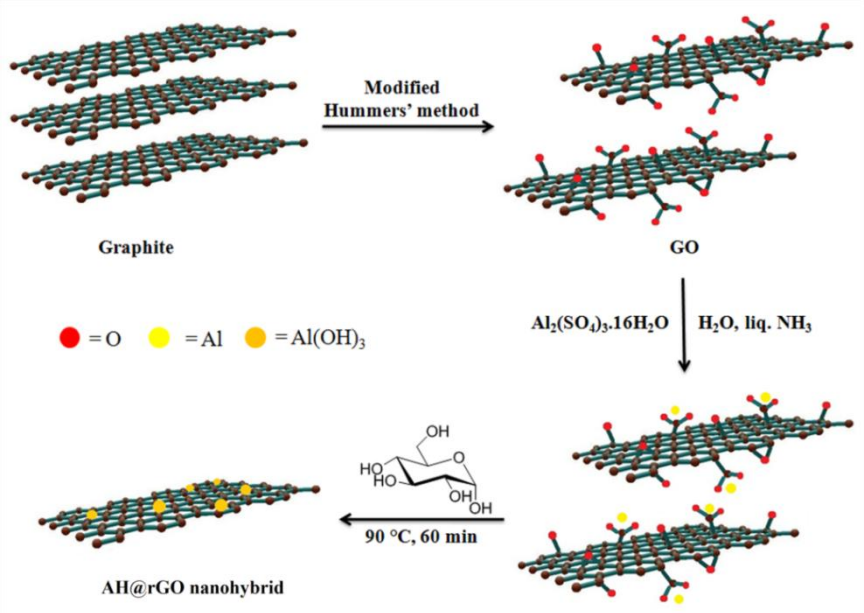

Scheme 3.1. Probable scheme for the formation of AH@rGO nanohybrid.

The initial process involved forming a proper aqueous dispersion of GO by ultrasonication which resulted in the exfoliation of the stacked graphitic sheets. The basal plane of GO sheets contains hydroxyl and epoxy groups, along with the carboxylic groups on the edges [2]. These oxygeneous functionalities significantly improved the dispersion of GO in water and facilitated the proper interaction between the Al precursors and the GO sheets. It is assumed that Al precursors undergo dative or ionic interactions with GO through these oxygeneous functionalities. These interactions, in turn, provided the support for the formation of $Al(OH)_3$ on rGO nano-sheets under alkaline conditions. These Al precursors deposited on the GO sheets act as sites of nucleation. These interactions are further augmented by the addition of aqueous ammonia. The role of ammonia was not only to convert Al precursors to $Al(OH)_3$ but also to achieve a controlled nucleation and crystal growth over the GO sheets. Reduction of GO was rapidly achieved by dextrose, in presence of ammonia [19]. In comparison, the reduction rate of GO tended to be slow without ammonia as detected in a control experiment. Hence, the introduction of ammonia favored the deoxygenation of GO and synergistically enhanced the rate of reduction of GO [20]. The reduction of GO resulted in the restoration of the aromatic conjugation of the graphitic domains and formation of AH@rGO nanohybrid system. The AH@rGO nanohybrid was

found to form stable dispersion in polar aprotic solvents like THF, DMF, DMAc, etc (**Figure 3.1**). This observation may stem from the fact that rGO nano-sheets, having highly conjugated electronic density, show strong electrostatic interactions with the polar aprotic media [21].

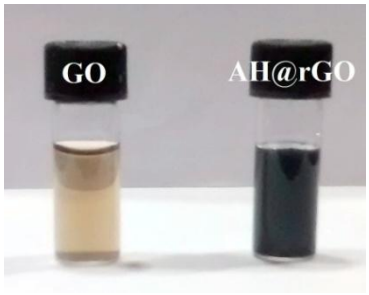

Figure 3.1. Digital image showing stable dispersion of GO and AH@rGO in DMF.

3.3.2. Characterization of AH@rGO nanohybrid

UV-Vis spectral analysis was indicative of the reduction of GO to rGO in the AH@rGO nanohybrid system (**Figure 3.2.a**). GO demonstrated characteristic absorbance bands at 236 nm and 300 nm corresponding to the $\pi \rightarrow \pi^*$ and $n \rightarrow \pi^*$ electronic transitions, respectively [18]. In AH@rGO, the absorbance band for $n \rightarrow \pi^*$ electronic transitions disappeared while the absorbance band for $\pi \rightarrow \pi^*$ electronic transitions was red-shifted to 277 nm, suggesting the removal of oxygeneous functional groups and formation of pure sp^2 hybridised graphitic domains of rGO [18]. FT-IR spectral analysis was useful in identifying the key changes during the reduction of GO to rGO and formation of the AH@rGO nanohybrid (**Figure 3.2.b**). In the FT-IR spectrum of GO, the appearance of sharp band at 3438 cm^{-1} can be ascribed to the presence of hydroxyl moieties on the surface of GO nano-sheets [18]. The asymmetric and symmetric stretching bands of C-H can be seen emerging near 2924 cm^{-1} and 2854 cm^{-1}. The medium band at 1625 cm^{-1} can be attributed to the skeletal vibrations of graphene domains, whereas a weak band for C=O stretching can be observed at 1744 cm^{-1} [18]. The C-H deformation band can be identified near 1460 cm^{-1}, while the C-O stretching band appeared prominently at 1022 cm^{-1}. In FT-IR spectrum of AH@rGO, broadening of the O-H band occurred indicating interactions between the residual hydroxyl groups and the $Al(OH)_3$ particles. Moreover, the sharpening of C=C stretching band and de-intensification of the C-H stretching and bending bands, both signify the restoration of the planar graphene domains. Further evidences of the formation of the nanohybrid can be offered by sharp bands at 1074 cm^{-1} and 478 cm^{-1} which can be attributed to Al-O stretching and bending vibrations [22, 23]. Raman scattering was quite helpful in detection of disorder in the graphitic structure of the nanohybrid. Two

fundamental vibration peaks *viz.* D band and G band were observed in range of 1100 cm^{-1} –1700 cm^{-1} in the Raman spectra of GO and AH@rGO, respectively (**Figure 3.2.c**). The AH@rGO system showed the D band at 1367 cm^{-1}, corresponding to the extent of disorder in graphitic domains; while the G band arising due to symmetric stretching of the graphitic sp^2 carbon of rGO appeared at 1617 cm^{-1} [18, 22]. On comparison with GO, the nanohybrid system displayed a blue shift in both the D and G bands, which may be due to nucleation of AH over rGO sheets. Moreover, the intensity ratio of the D band to the G band (I_D/I_G) increased slightly from 0.96 to 1.09 in nanohybrid system, which pointed towards the increase in the disorder of the graphitic domains due to the decoration of $Al(OH)_3$ on the surface of rGO nano-sheets and formation of AH@rGO. These observations are consistent with the previous literatures and suggested the formation of AH@rGO [24, 25]. The EDX mapping analysis (**Figure 3.2.d**) validated the presence of C, O and Al in the nanohybrid system with atomic and weight ratios of 65.09, 32.07, 2.79 and 56.93, 37.36, 5.48, respectively.

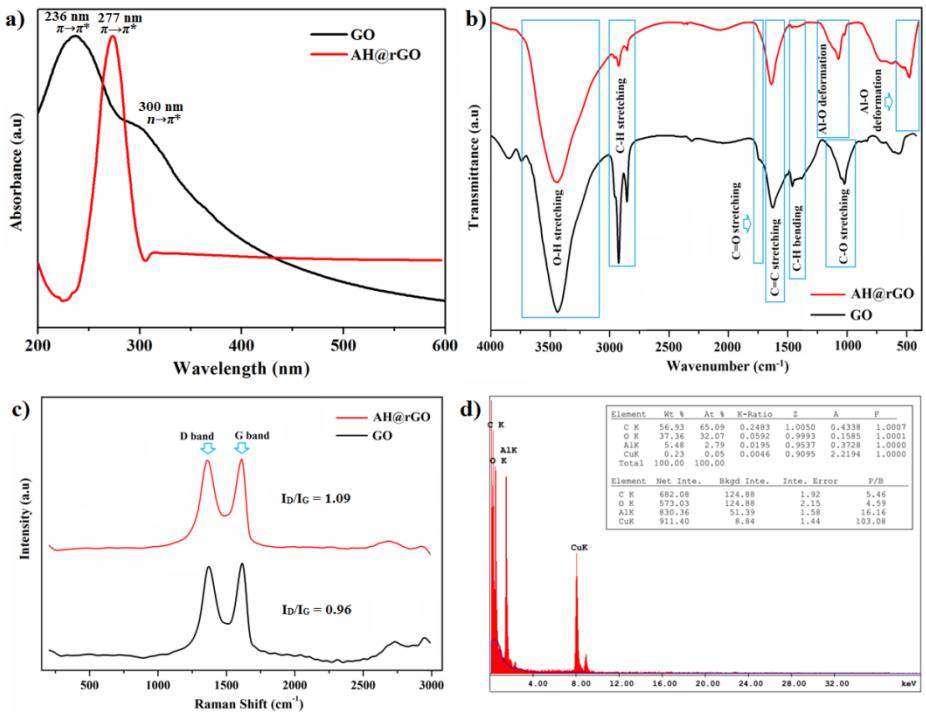

Figure 3.2. a) UV-Vis spectra of GO and AH@rGO, **b)** FT-IR spectra of GO and AH@rGO, **c)** Raman spectra of GO and AH@rGO, and **d)** EDX map of AH@rGO.

Morphological study of the nanohybrid by TEM presented sufficient evidence in favor of the prepared nanohybrid. TEM images clearly revealed the presence of $Al(OH)_3$ nanoparticles decorated over rGO nano-sheets (**Figure 3.3.a**). The rGO nano-sheets displayed a stacked appearance, due to possible agglomeration of the electronically

charged, large surfaced layers via. π–π stacking interactions. TEM images also suggested that the $Al(OH)_3$ nanoparticles possess nearly unsymmetrical spherical shape. Further, HRTEM of AH@rGO sheets displayed the presence of lattice fringes. Conversion of the selected areas in Figure 5b to corresponding IFFT images revealed two different inter-planar spacing of 0.218 nm and 0.246 nm for $Al(OH)_3$ phase, which may be attributed to occurrence of two different polymorphs of $Al(OH)_3$: gibbsite and bayerite (**Figure 3.3.b**). Also, HRTEM showed the presence of lattice fringes on rGO sheets. Corresponding IFFT conversion of a selected area divulged inter-planar spacing of 0.307 nm (**Figure 3.3.c**). Selected area diffraction (SAED) pattern of the nanohybrid exhibited concentric rings composed of several bright diffraction spots, indicating polycrystallinity in the structure (**Figure 3.3.d**).

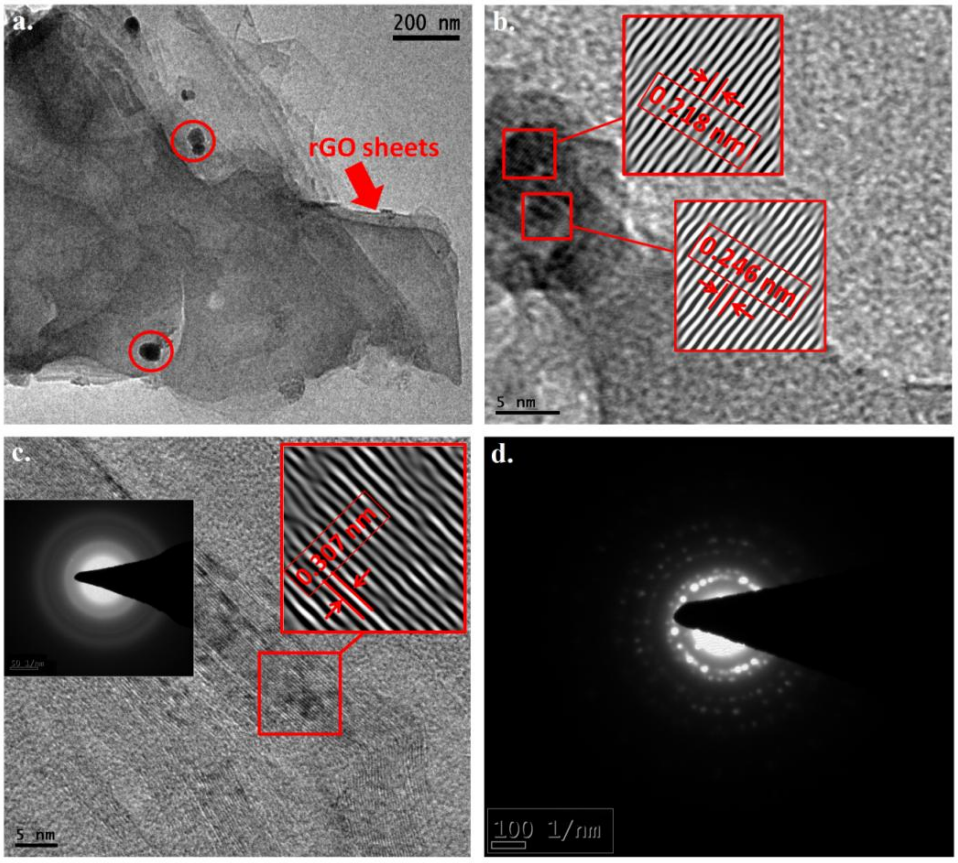

Figure 3.3. a) TEM image of AH@rGO showing $Al(OH)_3$ over rGO sheets, **b)** HR-TEM image of $Al(OH)_3$ phase (inset IFFT images showing inter-planar spacing of $Al(OH)_3$ phase), **c)** HR-TEM image of rGO sheets displaying lattice fringes (inset SAED pattern of rGO on left; inter-planar spacing of rGO phase on right), and **d)** SAED pattern of AH@rGO.

3.3.3. Fabrication of HPU/AH@rGO nanocomposite

HPU/AH@rGO nanocomposite was prepared by using an *in situ* polymerization technique.

Multi-functional moiety castor oil modified polyol was employed as the branch generating unit, and AH@rGO nanohybrid was used as the nano-reinforcing material, as shown in **Scheme 3.2**.

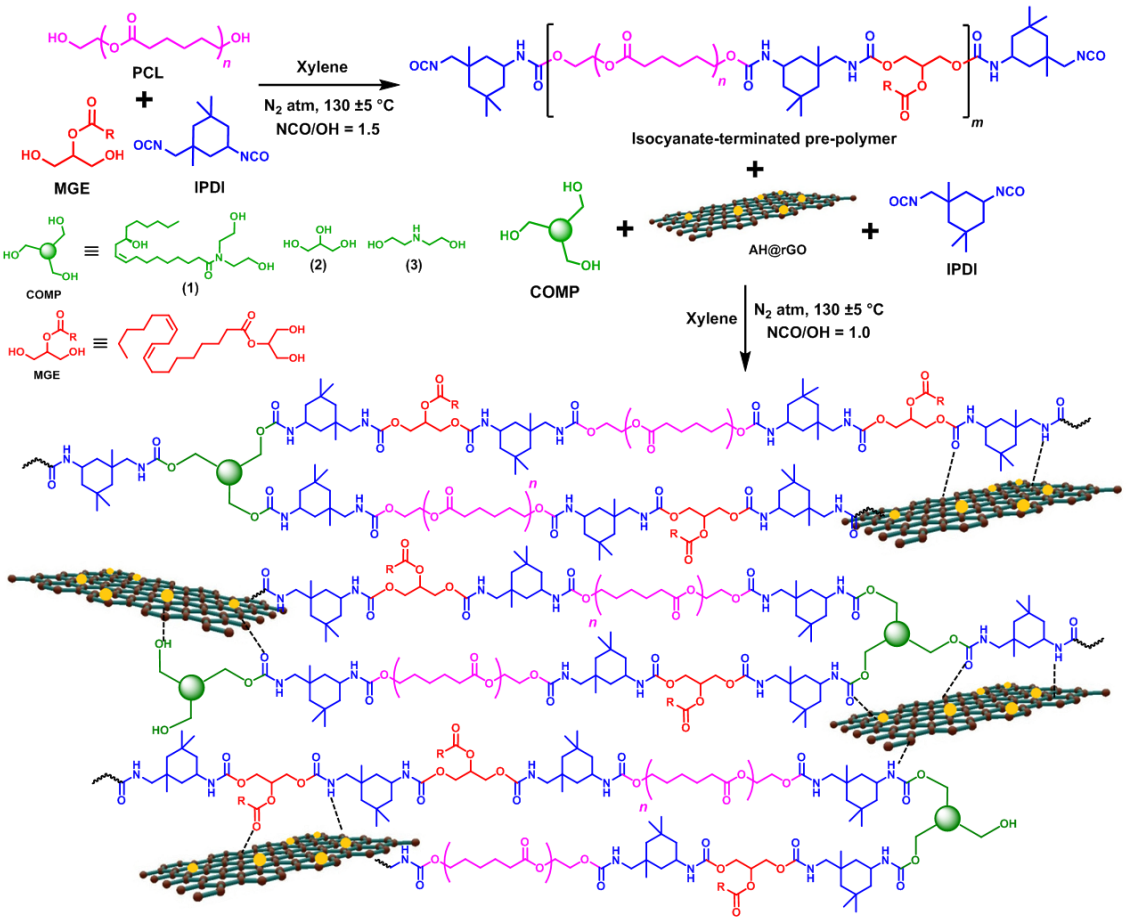

Scheme 3.2. Fabrication of HPU/AH@rGO nanocomposite.

An essential factor for the preparation of a nanocomposite is the compatibility and dispersibility of the nanomaterial in the polymer matrix, as it significantly influences the properties of the nanocomposite [26]. In this regard, HPU matrix was found to be suitable for the fabrication of the nanocomposite. HPU contains a large number of surface functionalities along its polymer network [27], which plays a key role in assimilating the nanohybrid. To ensure the formation of a uniform homogeneously distributed HPU/AH@rGO nanocomposite, a stable dispersion of the nanohybrid was introduced in the second step. In this way, the nanohybrid gets integrated easily in the HPU matrix during the polymerization reaction by strong physico-chemical interactions with the polymeric chains [28]. In this study, both the polymer matrix and the nanohybrid harmonized together to achieve a uniformly dispersed, highly compatible system. Another important factor to be considered is the concentration of the multi-functional moiety during polymerization. The

multi-functional moiety was administered slowly dropwise as a very dilute solution (15% in xylene) in the second step and maintained at 60% dilution (in xylene) to avoid gel formation until the end of the reaction [27].

3.3.4. Characterization of HPU/AH@rGO nanocomposite

The FT-IR study of the nanocomposite indicated the presence of key functional groups supporting the formation of the nanocomposite, especially the hyperbranched polyurethane matrix (**Figure 3.4.a**). Prominent vibrational frequencies such as N–H stretching at 3441 cm^{-1}, C=O stretching (of amide) at 1640 cm^{-1} and C–N stretching at 1020 cm^{-1} confirmed the presence of urethane linkages in the nanocomposite [27]. Other vibrational bands included C–H stretching at 2923 cm^{-1} and 2851 cm^{-1} and C=O stretching (of ester) at 1750 cm^{-1} and the N–H deformation band at 642 cm^{-1}. A medium peak of 467 cm^{-1} attributed to Al–O deformation suggested the fabrication of the AH@rGO nanohybrid over the HPU matrix [29]. Due to the very low nanohybrid content used during fabrication, the rest of the vibrational bands of the nanohybrid were overwhelmed by the polymer matrix. Also, it is relevant to mention here that the polyurethane matrix contains various polar functionalities which are susceptible to absorption of some amount of moisture. In this study, the O–H stretching band was eclipsed by the more prominent N–H stretching band due to the presence of strong urethane linkages and the close proximity of both their stretching frequencies. The XRD analysis of the nanocomposite (**Figure 3.4.b**) divulged the presence of crystallinity in their structure. The nanocomposites exhibited two distinct peaks at $2\theta = 20.7°$ (*d*-spacing of 4.65 Å) and 23° (*d*-spacing of 4.18 Å), corresponding to the (200) and (110) planes of the PCL moiety, respectively [26, 27]. Also, no additional peaks were observed for the AH@rGO nanohybrid in the XRD patterns of the nanocomposites. This implies the absence of long-range order of the nanohybrid in the HPU matrix. The presence of a small amount of the nanohybrid in the nanocomposites may also be the reason for this fact. In addition, increment of the peak intensity with nanomaterial loading was observed due to enhanced interaction between the nanohybrid and HPU matrix [14]. Moreover, the shifting of the PCL peaks towards higher angles suggested the formation of a compact structure. The surface morphology of the fractured nanocomposite films was visualized by SEM. SEM micrographs of the fractured surface (**Figure 3.5.a** and **Figure 3.5.b**) clearly reveal a microrough exterior with multiple layering, possibly due to intercalation and interactions of the HPU matrix in between the rGO sheets of the nanohybrid [26, 30]. The performance of the nanocomposites is largely dependent on the dispersion of the nanomaterial in the polymer matrix and their interfacial interactions. TEM analysis was employed to study the dispersion of the nanohybrid in the polymer

matrix. The TEM images clearly depicted a fine picture of some physico-chemical interactions of the HPU matrix with the AH@rGO sheets (**Figure 3.5.c**). The HRTEM images clearly showed the dispersion of AH@rGO in the HPU matrix (**Figure 3.5.d**).

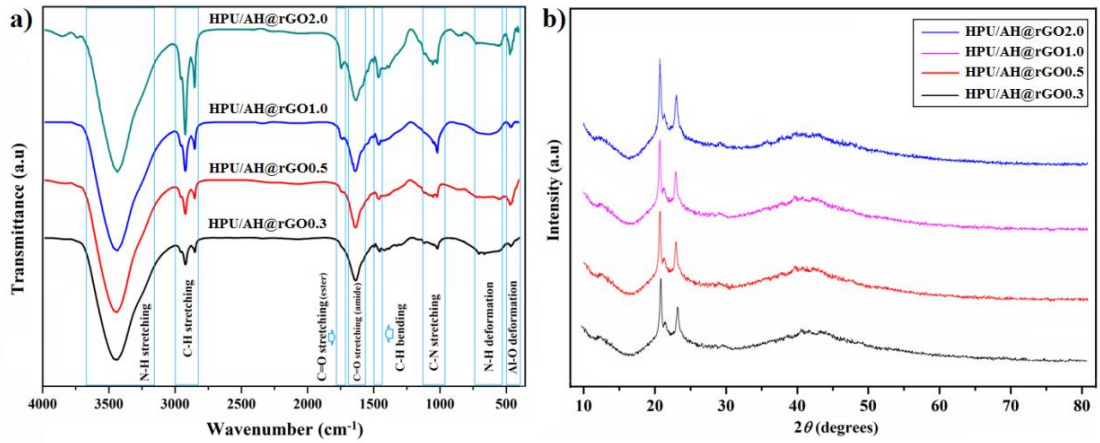

Figure 3.4. a) FT-IR spectra of HPU/AH@rGO nanocomposites, and **b)** XRD patterns of HPU/AH@rGO nanocomposites

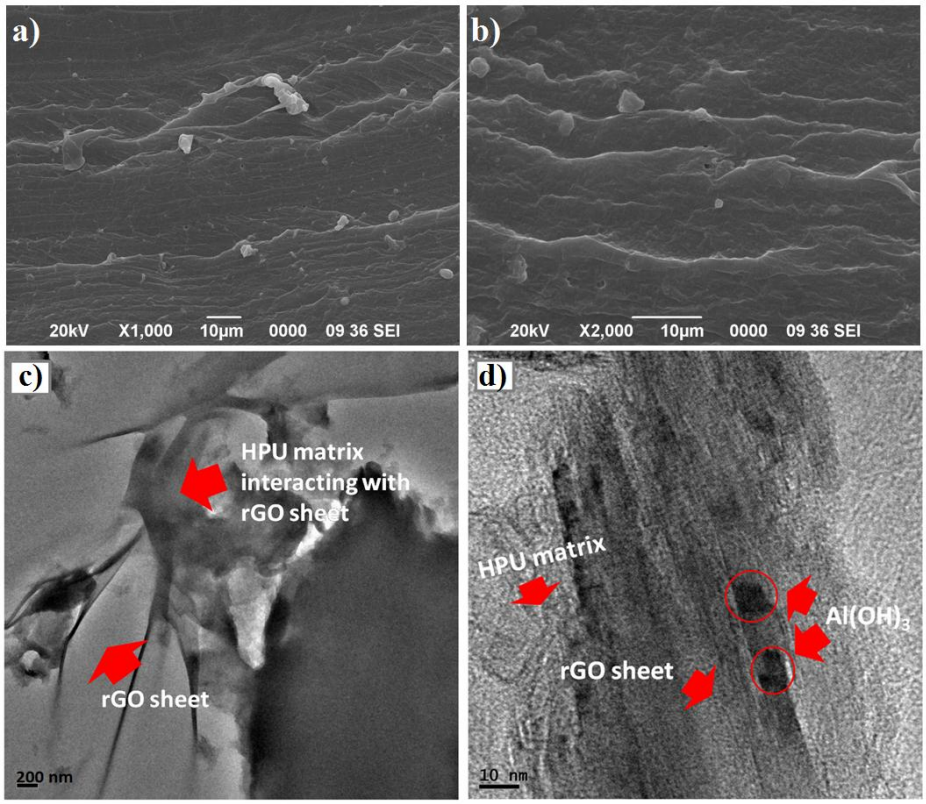

Figure 3.5. SEM micrographs of HPU/AH@RGO0.5 at 10 μm with **a)** 1000× magnification and **b)** 2000× magnification, TEM images of HPU/AH@RGO0.5 at magnification of **c)** 200 nm and **d)** 10 nm.

3.3.5. Mechanical properties

Various mechanical properties of the nanocomposites were evaluated and tabulated in **Table 3.1**. All the nanocomposites exhibited excellent mechanical properties like tensile strength (σ), elongation at break (ε), toughness (T), scratch hardness, and impact strength. The incorporation of the nanohybrid in the HPU matrix augmented the performance of the polymer *via* strong interfacial interactions between the polymeric chains and homogeneously dispersed nanohybrid. The nanocomposites showed huge improvement in the values of σ, ε, and T, in comparison to pristine HPU at very low loading of the nanohybrid. The stress-strain profiles of the nanocomposites are shown in **Figure 3.6.**

Table 3.1. Mechanical properties of HPU and its nanocomposites

Parameter	HPU/ AH@rGO0.3	HPU/ AH@rGO0.5	HPU/ AH@rGO1.0	HPU/ AH@rGO2.0	HPU
Tensile strength, σ (MPa)	10.5±0.5	13.7±0.4	17.7±0.2	7.9±0.4	5.1±0.2
Elongation at break, ε (%)	1318.5±10	1088.5±20	1018.7±10	1770.0±20	605.6±10
Toughness[a], T (MJm^{-3})	99.68±0.2	117.59±0.5	123.02±0.2	117.18±0.5	27.85±0.2
Scratch hardness[b] (kg)	>10	>10	>10	>10	>10
Impact strength[c] (kJm^{-1})	>19.02	>19.02	>19.02	>19.02	>19.02

[a]Calculated by integrating the stress-strain curves. [b]The maximum limit of scratch hardness was 10 kg. [c]The maximum limit of impact strength was 19.02 kJm^{-1} for the instrument.

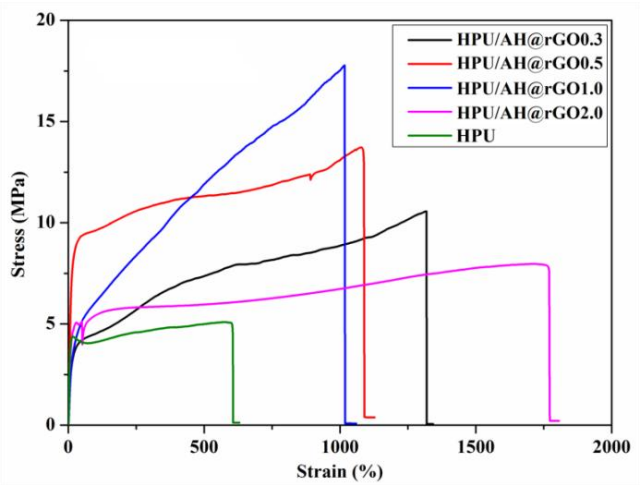

Figure 3.6. Stress-strain profiles of HPU/AH@RGO nanocomposites.

Various state-of-the-art literature reports have supported this enhancement of mechanical properties of PUNC with different contents of graphene composites [26, 28, 30]. The tensile strength of the nanocomposites showed a very high enhancement of ~350% upto 1 wt% loading of nanohybrid. Ideal compatibility and strong interfacial adhesion between the HPU matrix and AH@rGO nanohybrid increased the rigidity of the system by reinforcing the hard segments. Further, multiple secondary interactions in the form of H-bonding, $\pi-\pi$ stacking, van der Waals' interaction enhanced the structural stiffness. This resulted in effective transfer of load between HPU matrix and graphene sheets, thereby resulting in such high σ values [31]. Interestingly, upon increasing the loading upto 2 wt%, σ reduced by ~155%. This anomaly can be assigned to high yield stress, which altered the hard segments without significant reorientation and alignment. Moreover, higher content of the nanohybrid in the HPU matrix may have caused agglomeration of the nanohybrid in the HPU matrix, due to $\pi-\pi$ stacking interactions among rGO sheets, culminating in improper reinforcement of the HPU matrix [32]. At the same time, elongation at break of the nanocomposites was found to be increased upto ~292% compared to pristine HPU at low nanomaterial content. This significant enhancement of ε can be ascribed to the mobility of rGO-reinforced polymeric chains. Literature reports that ε follows a complex behavior with different graphene contents in PUNCs. Experimental results by Chen *et al*. showed that the nanocomposites maintain ε almost equivalent to that of pristine polyurethane [33]. Reports from Wu *et al.* showed a continuous decrease in ε upon increase in the content of graphene, whereas Thakur *et al.* found a constant increase in ε with increasing graphene content [28, 32]. Zhang *et al.* reported an irregular trend of ε with graphene content that increased up to an optimized loading and then went decreasing [34]. In our investigation, a similar irregular trend was observed. ε values were found to follow a steady receding pattern, going from ~215% to ~165% upto 1 wt% content of nanohybrid. The low elongation at higher loading can be credited to the aggregation of rGO sheets in the HPU matrix, effecting in a stress concentration near the reinforced hard segments in the stretching process. Moreover, as rGO sheets preferentially reinforced the hard segments, rigidity of the soft segments remained intact [36]. However, surprisingly further increment of nanohybrid loading to 2 wt% led to the sudden increase of ε% to ~292%. This result is difficult to explain at this moment, though it may have been resulted from the high nanohybrid content in the matrix, which imparted unusual elongation *via.* full extension of polymer chains along the loading direction and sliding of agglomerated rGO layers past one another by lengthening its $\pi-\pi$ stacking interactions [15, 26, 30]. The nanocomposite also recorded a sequential enhancement in toughness upto ~441%, with increasing nanohybrid content upto 1 wt%, followed by slight decline to 420% upon 2 wt% loading. Since

toughness of the material is a combination of its rigidity and flexibility, hence the synergistic effect of stiffness of the rGO reinforced polymer segments and mobility of the covalently/non-covalently rGO-bound polymeric chains contributed to this dramatic result [26, 30].

3.3.6. Thermal properties

Thermal study revealed information pertaining to the thermo-stability of the nanocomposites. The TG thermograms of the nanocomposites are shown in **Figure 3.7** and the different thermal parameters are tabulated in **Table 3.2.**

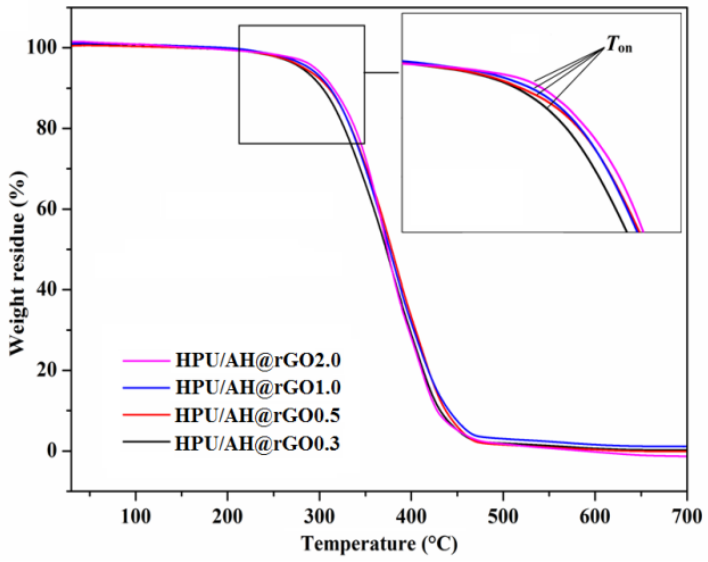

Figure 3.7. TG thermograms of HPU/AH@rGO nanocomposites.

Table 3.2. Thermal degradation temperatures of HPU/AH@rGO nanocomposites

Parameter	HPU/ AH@rGO0.3	HPU/ AH@rGO0.5	HPU/ AH@rGO1.0	HPU/ AH@rGO2.0
Onset decomposition temperature, T_{on} (°C)	300	306	308	315
Maximum decomposition temperature, T_{max} (°C)	375	375	377	378
End-decomposition temperature, T_{end} (°C)	430	437	442	446

All the nanocomposites showed high thermal resistance to degradation, with slight enhancement of the degradation temperature, corresponding to increase in loading of the

nanohybrid (Table 3.2). Such enhancement can be attributed to the presence of AH decorated rGO nano-sheets in the polymer matrix. These graphene sheets acted as nano-fillers, occupying free volume in the polymer matrix and made the system more rigid *via.* covalent or non-covalent interactions with the polymer chains. This led to the limited thermal motion of molecular chains, resulting in enhanced thermal stability. State of art literature has supported this enhancement in thermal stability of PU/graphene nanocomposites [4, 6, 26, 30]. Moreover, the presence of thermally insulating aluminium hydroxide substantially contributed to this thermo-stability [29, 37, 38].

Again, the DSC study provided more information about the thermal behaviour of the nanocomposites. The DSC curves are illustrated in **Figure 3.8** and the corresponding parameters are tabulated in **Table 3.3**. The glass transition temperature of the soft segments (T_g) displayed no variation, while that of the hard segments ($T_{g'}$) displayed an increasing trend with nanohybrid content. This indicated the preferential confinement of the hard segments by the graphene nano-sheets. On a similar note, the melting transition temperature (T_m) of the nanocomposites demonstrated an increasing trend with increasing nanohybrid content. As the nanohybrid content increased, the nucleating ability of graphene sheets restricted the mobility of the polymer chains [39]. Such temperature enhancement with nanohybrid loading has also been supported by TG analysis. Similar observations have been reported by Mahapatra et al. [40], as well as by Pokharel et al. [41], for functionalized graphene/PUNC system.

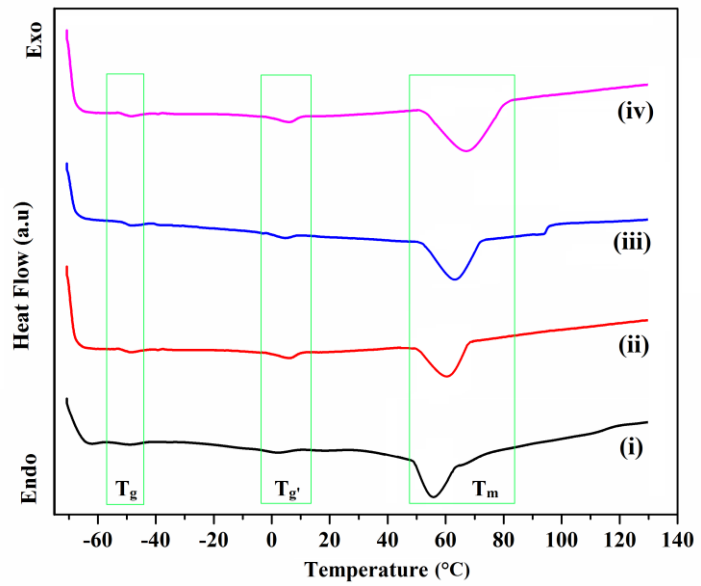

Figure 3.8. DSC curves of (i) HPU/AH@rGO0.3, (ii) HPU/AH@rGO0.5, (iii) HPU/AH@rGO01.0, and (iv) HPU/AH@rGO2.0.

Table 3.3. Thermal transition temperature of HPU/AH@rGO nanocomposites

Parameter	HPU/ AH@rGO0.3	HPU/ AH@rGO0.5	HPU/ AH@rGO1.0	HPU/ AH@rGO2.0
Glass transition temperature of soft segments, T_g (°C)	−52.0	−52.3	−52.0	−52.1
Glass transition temperature of hard segments, $T_{g'}$ (°C)	−4.0	−0.5	1.5	2.0
Melting transition temperature, T_m (°C)	56.7	62.0	63.5	68.7

3.3.7. Shape memory study

Shape memory behavior of a material is an entropic effect [41]. The polymeric chains of the nanocomposite are oriented in a random fashion under ambient conditions, implying a state of maximum entropy. Upon heating the polymer system at the switching temperature, the activation of polymer chain mobility occurs [14]. Application of an external force results in the temporary conformational deformity of the system. All the chains experience the same amount of deformation on application of external force and this deformation is memorized by the polymeric chains. The entire process is accompanied by lowering of entropy of the system by freezing the polymer in ice cold water-salt solution. This results in fixation of the temporary shape of the polymer. Ultimately, this temporary shape was successfully reverted to original shape by application of different stimuli. The recovery of the original shape is caused by the re-activation of the polymer chain mobility, by triggering its switching temperature [14, 19]. For optimum results, the switching temperature was chosen to be 60(±5) °C, which is very close to the melting transition temperature, T_m of the soft segments.

All the compositions of nanocomposites demonstrated outstanding multi-stimuli triggered shape memory behavior under thermal heating, microwave and sunlight. The nanocomposites exhibited excellent shape fixity as well as shape recovery. The shape memory behaviors of the nanocomposite by thermal heating and sunlight are shown in **Figure 3.9**. The shape recovery time and percentages under different stimuli are tabulated in **Table 3.4**. Shape recovery values of the nanocomposite films were to be proficient upon exposure to MW and sunlight, apart from direct thermal stimulus. This can be credited to the presence of AH-rGO nanohybrid within the HPU matrix. The HPU matrix with its unique

hyperbranched structural feature of inherent hard-soft segments and the nanohybrid containing rGO sheets, acting as a nanoheater, effectively combined together to give an effective shape memory action. The radiation absorbed by this uniformly distributed nanohybrid triggered an effective thermal energy disbursement throughout the polymer matrix. This resulted in an efficient transfer of stored elastic strain energy from nanohybrid to the HPU matrix. This facilitated the nanocomposite system in attaining a high recovery speed by the release of the stored elastic strain. The overall study showed thermal heating at 60(±5) °C to be the optimum stimulus for shape recovery. Also, MW irradiation at 300 W was adequate enough to trigger good shape recovery. However, shape recovery took a longer time under direct sunlight than the rest. In all the cases, the shape-recovery time decreased with the increase of nanohybrid content in the nanocomposites.

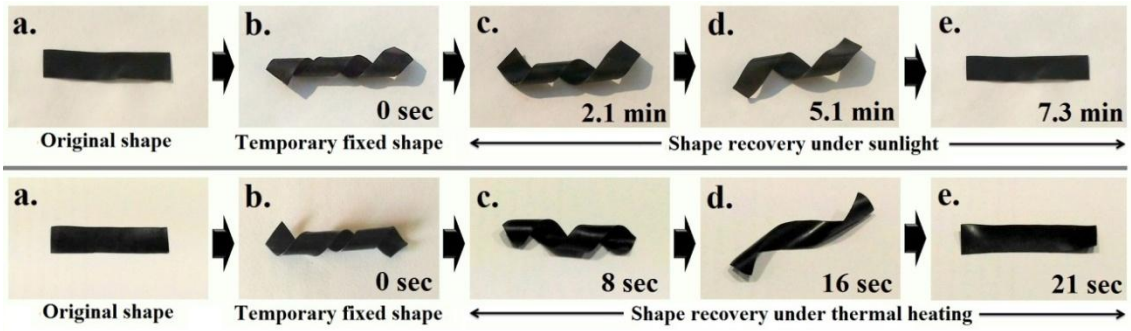

Figure 3.9. Shape memory behavior of HPU-AH-rGO2.0 under thermal heating and sunlight.

Table 3.4. Shape memory features of the HPU/AH@rGO nanocomposites

Stimulus		HPU/ AH@rGO0.3	HPU/ AH@rGO0.5	HPU/ AH@rGO1.0	HPU/ AH@rGO2.0
Thermal	Shape recovery time (s)	28	27	23	21
	Shape recovery (%)	96.8	96.9	96.8	97.1
MW	Shape recovery time (s)	120	110	97	90
	Shape recovery (%)	96.7	96.9	97.3	98.4
Sunlight	Shape recovery time (min)	9.3	9.1	8.0	7.3
	Shape recovery (%)	93.4	93.5	94.8	95.3

3.4. Conclusion

The current chapter describes the utility of AH@rGO nanohybrid as a reinforcing material for fabrication of HPUNC. HPUNC with varying loadings of the nanohybrid was successfully prepared by an *in situ* polymerization technique. The nanohybrid was found to be easily compatible with the polymer matrix. The study revealed that the nanocomposites possess high mechanical properties and thermal stability. In addition, the nanocomposite system exhibited multi-stimuli responsive shape memory behavior. The presence of AH@rGO nanohybrid enhanced the thermo-stability and shape memory behavior of the nanocomposite. Sunlight and microwave irradiation, along with thermal energy was successfully utilized as trigger stimuli. Such a system can be vital in the development of eco-friendly, high performance material for potential smart applications.

References

[1] Cai, D. and Song, M. Recent advance in functionalized graphene/polymer nanocomposites. *Journal of Materials Chemistry*, 20(37):7906–7915, 2010.

[2] Ramanathan, T., Abdala, A. A., Stankovich, S., Dikin, D. A., Herrera-Alonso, M., Piner, R. D., Adamson, D. H., Schniepp, H. C., Chen, X. R. R. S., Ruoff, R. S., and Nguyen, S. T. Functionalized graphene sheets for polymer nanocomposites. *Nature Nanotechnology*, 3(6):327, 2008.

[3] Novoselov, K. S., Geim, A. K., Morozov, S. V., Jiang, D., Zhang, Y., Dubonos, S. V., Grigorieva, I. V., and Firsov, A. A. Electric field effect in atomically thin carbon films. *Science*, 306(5696):666-669, 2004.

[4] Wang, X., Hu, Y., Song, L., Yang, H., Xing, W., and Lu, H. In situ polymerization of graphene nanosheets and polyurethane with enhanced mechanical and thermal properties. *Journal of Materials Chemistry*, 21(12):4222-4227, 2011.

[5] Kim, H., Miura, Y., and Macosko, C. W. Graphene/polyurethane nanocomposites for improved gas barrier and electrical conductivity. *Chemistry of Materials*, 22(11):3441-3450, 2010.

[6] Strankowski, M., Korzeniewski, P., Strankowska, J., AS, A., and Thomas, S. Morphology, mechanical and thermal properties of thermoplastic polyurethane containing reduced graphene oxide and graphene nanoplatelets. *Materials*, 11(1):82, 2018.

[7] Walker, L. S., Marotto, V. R., Rafiee, M. A., Koratkar, N., and Corral, E. L. Toughening in graphene ceramic composites. *ACS Nano*, 5(4):3182-3190, 2011.

[8] Chou, S. L., Wang, J. Z., Choucair, M., Liu, H. K., Stride, J. A., and Dou, S. X. Enhanced reversible lithium storage in a nanosize silicon/graphene composite. *Electrochemistry Communications*, 12(2):303-306, 2010.

[9] Centeno, A., Rocha, V. G., Alonso, B., Fernández, A., Gutierrez-Gonzalez, C. F., Torrecillas, R., and Zurutuza, A. Graphene for tough and electroconductive alumina ceramics. *Journal of the European Ceramic Society*, 33(15-16):3201-3210, 2013.

[10] Thakur, S. and Hu, J. Polyurethane: A shape memory polymer (SMP). In Yilmaz, F., editor, *Aspects of Polyurethanes*, pages 53-54. IntechOpen, London, UK, 2017.

[11] Meng, H. and Li, G. A review of stimuli-responsive shape memory polymer composites. *Polymer*, 54(9):2199-2221, 2013.

[12] Sahoo, N. G., Jung, Y. C., Yoo, H. J., and Cho, J. W. Influence of carbon nanotubes and polypyrrole on the thermal, mechanical and electroactive shape-memory properties of polyurethane nanocomposites. *Composites Science and Technology*, 67(9):1920-1929, 2007.

[13] Hager, M. D., Bode, S., Weber, C., and Schubert, U. S. Shape memory polymers: past, present and future developments. *Progress in Polymer Science*, 49:3-33, 2015.

[14] Thakur, S. and Karak, N. Bio-based tough hyperbranched polyurethane–graphene oxide nanocomposites as advanced shape memory materials. *RSC Advances*, 3(24):9476-9482, 2013.

[15] Jung, Y. C., Kim, J. H., Hayashi, T., Kim, Y. A., Endo, M., Terrones, M., and Dresselhaus, M. S. Fabrication of transparent, tough, and conductive shape-memory polyurethane films by incorporating a small amount of high-quality graphene. *Macromolecular Rapid Communications*, 33(8):628-634, 2012.

[16] Han, S. and Chun, B. C. Preparation of polyurethane nanocomposites via covalent incorporation of functionalized graphene and its shape memory effect. *Composites Part A: Applied Science and Manufacturing*, 58:65-72, 2014.

[17] Kim, J. T., Kim, B. K., Kim, E. Y., Park, H. C., and Jeong, H. M. Synthesis and shape memory performance of polyurethane/graphene nanocomposites. *Reactive and Functional Polymers*, 74:16-21, 2014.

[18] Thakur, S. and Karak, N. Green reduction of graphene oxide by aqueous phytoextracts. *Carbon*, 50(14):5331-5339, 2012.

[19] Zhu, C., Guo, S., Fang, Y., and Dong, S. Reducing sugar: new functional molecules for the green synthesis of graphene nanosheets. *ACS Nano*, 4(4):2429-2437, 2010.

[20] Fan, X., Peng, W., Li, Y., Li, X., Wang, S., Zhang, G., and Zhang, F. Deoxygenation of exfoliated graphite oxide under alkaline conditions: a green route to graphene preparation. *Advanced Materials*, 20(23):4490-4493, 2008.

[21] Konios, D., Stylianakis, M. M., Stratakis, E., and Kymakis, E. Dispersion behaviour of graphene oxide and reduced graphene oxide. *Journal of Colloid and Interface Science*, 430:108-112, 2014.

[22] Dubovoy, V., Stranick, M., Du-Thumm, L., and Pan, L. Development of ambient nanogibbsite synthesis and incorporation of the method to embed ultrafine nano-$Al(OH)_3$ into channels and partial alumination of MCM-41. *Crystal Growth & Design*, 16(3):1717-1724, 2016.

[23] Barathi, M., Kumar, A. S. K., Kumar, C. U., and Rajesh, N. Graphene oxide–aluminium oxyhydroxide interaction and its application for the effective adsorption of fluoride. *RSC Advances*, 4(96):53711-53721, 2014.

[24] Stankovich, S., Dikin, D. A., Piner, R. D., Kohlhaas, K. A., Kleinhammes, A., Jia, Y., Wu, Y., Nguyen, S. T., and Ruoff, R. S. Synthesis of graphene-based nanosheets via chemical reduction of exfoliated graphite oxide. *Carbon*, 45(7):1558-1565, 2007.

[25] Zhou, Y., Bao, Q., Tang, L. A. L., Zhong, Y., and Loh, K. P. Hydrothermal dehydration for the "green" reduction of exfoliated graphene oxide to graphene and demonstration of tunable optical limiting properties. *Chemistry of Materials*, 21(13):2950-2956, 2009.

[26] Thakur, S. and Karak, N. Ultratough, ductile, castor oil-based, hyperbranched, polyurethane nanocomposite using functionalized reduced graphene oxide. *ACS Sustainable Chemistry & Engineering*, 2(5):1195-1202, 2014.

[27] Bayan, R. and Karak, N. Renewable resource modified polyol derived aliphatic hyperbranched polyurethane as a biodegradable and UV-resistant smart material. *Polymer International*, 66(6):839-850, 2017.

[28] Thakur, S. and Karak, N. Multi-stimuli responsive smart elastomeric hyperbranched polyurethane/reduced graphene oxide nanocomposites. *Journal of Materials Chemistry A*, 2(36):14867-14875, 2014.

[29] Jankovský, O., Šimek, P., Sedmidubský, D., Huber, Š., Pumera, M., and Sofer, Z. Towards highly electrically conductive and thermally insulating graphene nanocomposites: Al_2O_3–graphene. *RSC Advances*, 4(15):7418-7424, 2014.

[30] Yadav, S. K. and Cho, J. W. Functionalized graphene nanoplatelets for enhanced mechanical and thermal properties of polyurethane nanocomposites. *Applied Surface Science*, 266:360-367, 2013.

[31] Chen, D., Zhu, H., and Liu, T. In situ thermal preparation of polyimide nanocomposite films containing functionalized graphene sheets. *ACS Applied Materials & Interfaces*, 2(12):3702-3708, 2010.

[32] Wu, C., Huang, X., Wang, G., Wu, X., Yang, K., Li, S., and Jiang, P. Hyperbranched-polymer functionalization of graphene sheets for enhanced mechanical and dielectric properties of polyurethane composites. *Journal of Materials Chemistry*, 22(14):7010-7019, 2012.

[33] Chen, Z. and Lu, H. Constructing sacrificial bonds and hidden lengths for ductile graphene/polyurethane elastomers with improved strength and toughness. *Journal of Materials Chemistry*, 22(25):12479-12490, 2012.

[34] Zhang, J., Zhang, C., and Madbouly, S. A. In situ polymerization of bio-based thermosetting polyurethane/graphene oxide nanocomposites. *Journal of Applied Polymer Science*, 132(13):41751, 2015.

[35] Pei, A., Malho, J. M., Ruokolainen, J., Zhou, Q., and Berglund, L. A. Strong nanocomposite reinforcement effects in polyurethane elastomer with low volume fraction of cellulose nanocrystals. *Macromolecules*, 44(11):4422-4427, 2011.

[36] Song, P., Cao, Z., Cai, Y., Zhao, L., Fang, Z., and Fu, S. Fabrication of exfoliated graphene-based polypropylene nanocomposites with enhanced mechanical and thermal properties. *Polymer*, 52(18):4001-4010, 2011.

[37] Wang, W., He, K., Dong, Q., Zhu, N., Fan, Y., Wang, F., Xia, Y., Li, H., Wang, J., Yuan, Z., and Wang, E. Synergistic effect of aluminum hydroxide and expandable graphite on the flame retardancy of polyisocyanurate–polyurethane foams. *Journal of Applied Polymer Science*, 131(4):39936, 2014.

[38] Furukawa, M. and Yokoyama, T. Mechanical properties of organic–inorganic polyurethane elastomers. I. $Al(OH)_3$–polyurethane composites based on PPG. *Journal of Applied Polymer Science*, 53(13):723-1729, 1994.

[39] Park, J., Dao, T., Lee, H. I., Jeong, H., and Kim, B. Properties of graphene/shape memory thermoplastic polyurethane composites actuating by various methods. *Materials*, 7(3):1520-1538, 2014.

[40] Mahapatra, S. S., Ramasamy, M. S., Yoo, H. J., and Cho, J. W. A reactive graphene sheet in situ functionalized hyperbranched polyurethane for high performance shape memory material. *RSC Advances*, 4(29):15146-15153, 2014.

[41] Pokharel, P., Pant, B., Pokhrel, K., Pant, H. R., Lim, J. G., Kim, H. Y., and Choi, S. Effects of functional groups on the graphene sheet for improving the thermomechanical properties of polyurethane nanocomposites. *Composites Part B: Engineering*, 78:192-201, 2015.